Supplementary Material for "Decadal Indian Ocean influence on the ENSO-Indian monsoon teleconnection mostly apparent"

1 Supplementary figures...

... Figs. S1-S13, with commentary in the figure captions.

2 A naive hypothesis of the connection of ENSO variability and mean IOD*

Considering R_{σ_N,I^*}, naively, it is a (apparent) mean state that can causally drive some (apparent) variability, not the other way round. As a first look at this matter, the ENSO-driven IOD model given by eq. (3) of [1] does not reproduce $R_{\sigma_N,I^*} = -0.43$ (Table 1), but rather yields – confirming some of our intuition – a small insignificant value using the 20th c. CESM2-LE Nino3.4 data (Methods). However, this toy model produces an unskewed I, whereas in reality, and in the CESM2-LE, I is negatively skewed, featuring heavier tails for -ve values of I. Considering eq. (3) and the intuitive correlation of variances, $R_{\sigma_N,\sigma_I} > 0$ (displayed certainly even by the toy model), we do expect $R_{\sigma_N,I} < 0$, and indeed have in the CESM2-LE. This already quashes our naive idea. Nevertheless, this is not the simple *statistical* explanation for $R_{\sigma_N,I^*} = -0.43$ as I^* – versus I – is not obviously skewed; "the decorrelation removed the skewness". This demonstration, if not its foreignness of sorts, highlights the other value in considering I^* instead of I.

3 A regional view of causality

As the apparent influence of the IO on ENSO variance seems to affect Eastern central India most strongly, we also investigate the causality wrt. the regression coefficient (i) (Fig. S14 (d,e)), too, and find a rather complex dynamics, *positive (negative) correlations in association with leading (lagging) the IO.* The causality wrt. local monsoon variability (iii.b) (Fig. 14 (f,g)), on the other hand, also shows IO dominance, locally, at stronger levels of the correlation, more pronounced than in the case of the areal mean AISMR (b). It is also a particular point of interest that the IO's dominant causal influence on the teleconnection via the monsoon variability (iii.b) is opposing in effect to the subdominant causal influence via ENSO variability (ii), which makes the IO's overall *causal* influence on the ENSO-ISM teleconnection less easy to articulate concisely.

References

[1] Malte F. Stuecker, Axel Timmermann, Fei-Fei Jin, Yoshimitsu Chikamoto, Wenjun Zhang, Andrew T. Wittenberg, Esther Widiasih, and Sen Zhao. Revisiting ENSO/Indian Ocean Dipole phase relationships. *Geophysical Research Letters*, 44(5):2481–2492, 2017.

[2] Mátyás Herein, János Márfy, Gábor Drótos, and Tamás Tél. Probabilistic Concepts in Intermediate-Complexity Climate Models: A Snapshot Attractor Picture. *Journal of Climate*, 29(1):259–272, 2016.

[3] Vineel Yettella, Jeffrey B. Weiss, Jennifer E. Kay, and Angeline G. Pendergrass. An Ensemble Covariance Framework for Quantifying Forced Climate Variability and Its Time of Emergence. *Journal of Climate*, 31(10):4117–4133, 2018.

[4] Tamás Bódai, Gábor Drótos, Mátyás Herein, Frank Lunkeit, and Valerio Lucarini. The Forced Response of the El Niño–Southern Oscillation–Indian Monsoon Teleconnection in Ensembles of Earth System Models. *Journal of Climate*, 33(6):2163–2182, 2020.

[5] K. B. Rodgers, S.-S. Lee, N. Rosenbloom, A. Timmermann, G. Danabasoglu, C. Deser, J. Edwards, J.-E. Kim, I. Simpson, K. Stein, M. F. Stuecker, R. Yamaguchi, T. Bodai, E.-S. Chung, L. Huang, W. Kim, J.-F. Lamarque, D. Lombardozzi, W. R. Wieder, and S. G. Yeager. Reply on RC1 (Ubiquity of human-induced changes in climate variability). *Earth System Dynamics Discussions*, 2021.

[6] K. B. Rodgers, S.-S. Lee, N. Rosenbloom, A. Timmermann, G. Danabasoglu, C. Deser, J. Edwards, J.-E. Kim, I. R. Simpson, K. Stein, M. F. Stuecker, R. Yamaguchi, T. Bódai, E.-S. Chung, L. Huang, W. M. Kim, J.-F. Lamarque, D. L. Lombardozzi, W. R. Wieder, and S. G. Yeager. Ubiquity of human-induced changes in climate variability. *Earth System Dynamics*, 12(4):1393–1411, 2021.

[7] Gábor Drótos, Tamás Bódai, and Tamás Tél. On the importance of the convergence to climate attractors. *The European Physical Journal Special Topics*, 226(9):2031–2038, 2017.

[8] Tamás Bódai and Tamás Tél. Annual variability in a conceptual climate model: Snapshot attractors, hysteresis in extreme events, and climate sensitivity. *Chaos: An Interdisciplinary Journal of Nonlinear Science*, 22(2):023110, 2012.

[9] Gábor Drótos, Tamás Bódai, and Tamás Tél. Probabilistic Concepts in a Changing Climate: A Snapshot Attractor Picture. *Journal of Climate*, 28(8):3275–3288, 2015.

[10] T. Tél, T. Bódai, G. Drótos, T. Haszpra, M. Herein, B. Kaszás, and M. Vincze. The Theory of Parallel Climate Realizations. *Journal of Statistical Physics*, 2019.

[11] Halbert White. A heteroskedasticity-consistent covariance matrix estimator and a direct test for heteroskedasticity. *Econometrica*, 48(4):817–838, 1980.

[12] Csernák Gábor and Stépán Gábor. *Rezgéstan.* Akadémiai Kiadó, 2019.

[13] Tamás Bódai, Gábor Drótos, Kyung-Ja Ha, June-Yi Lee, and Eui-Seok Chung. Nonlinear Forced Change and Nonergodicity: The Case of ENSO-Indian Monsoon and Global Precipitation Teleconnections. *Frontiers in Earth Science*, 8:729, 2021.

[14] K. Takahashi, A. Montecinos, K. Goubanova, and B. Dewitte. ENSO regimes: Reinterpreting the canonical and Modoki El Niño. *Geophysical Research Letters*, 38(10), 2011.

[15] Wenjun Zhang, Yalan Wang, Fei-Fei Jin, Malte F. Stuecker, and Andrew G. Turner. Impact of different El Niño types on the El Niño/IOD relationship. *Geophysical Research Letters*, 42(20):8570–8576, 2015.

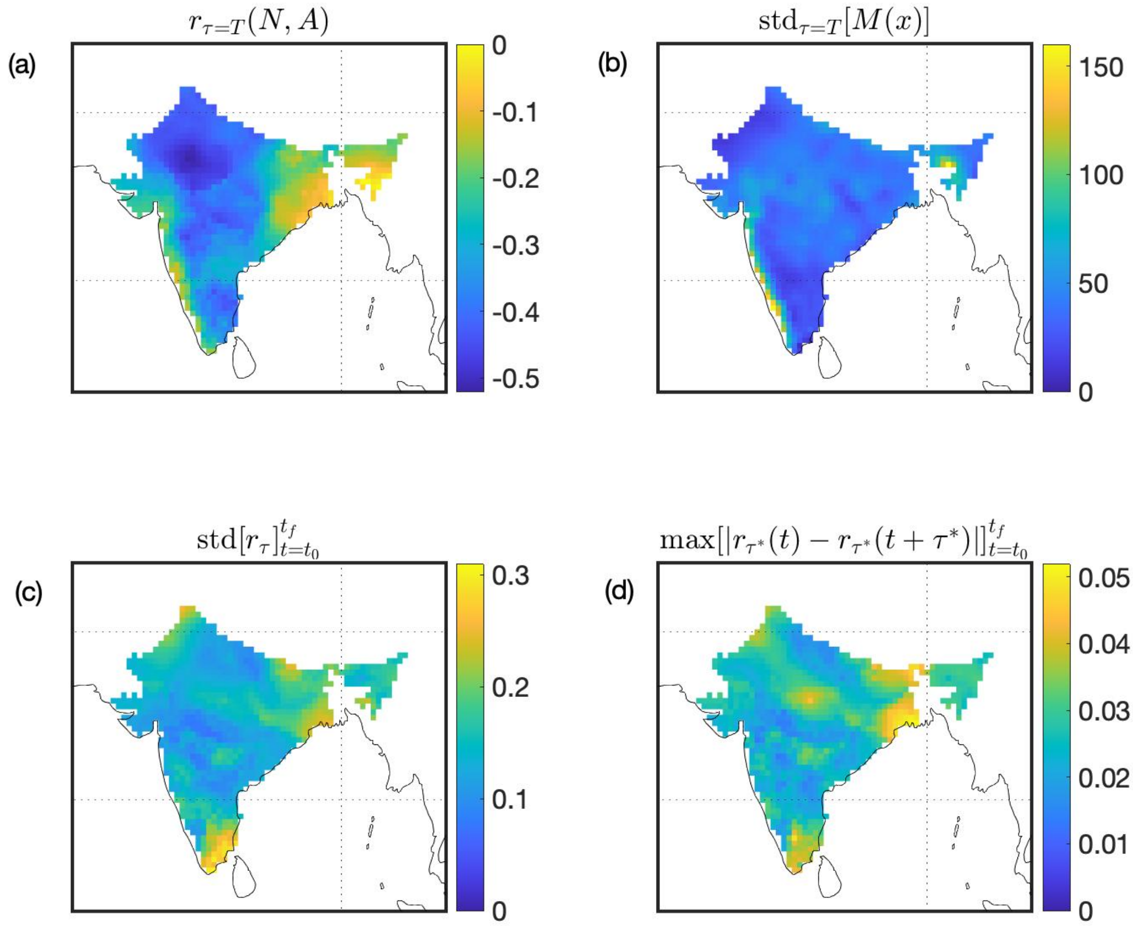

Figure S 1: Aspects of the observational data, as a supplemental figure to Fig. 1. (a) Overall 20th c. correlation coefficient $r_{\tau=T}(N, M(x))$ and (b) monsoon variability $\sigma_{\tau=T}(M(x))$, $T = t_f - t_0 = 100$, $t_0 = 1901$, $t_f = 2000$ [yr] (upon detrending), representing the null-hypothesis H_0 (8). (c) and (d) show the values taken by the two alternative test statistics, $\mathrm{std}[r_\tau]_{t=t_0}^{t_f}$, $\tau = 20$ [yr] (for T1), and $\max[|r_{\tau^*}(t) - r_{\tau^*}(t+\tau^*)|]_{t=t_0}^{t_f}$, $\tau^* = \tau = 20$ [yr] (for T2), respectively. Similar patterns of these coincide with the similarity of those of the associated p-values in Fig. 1.

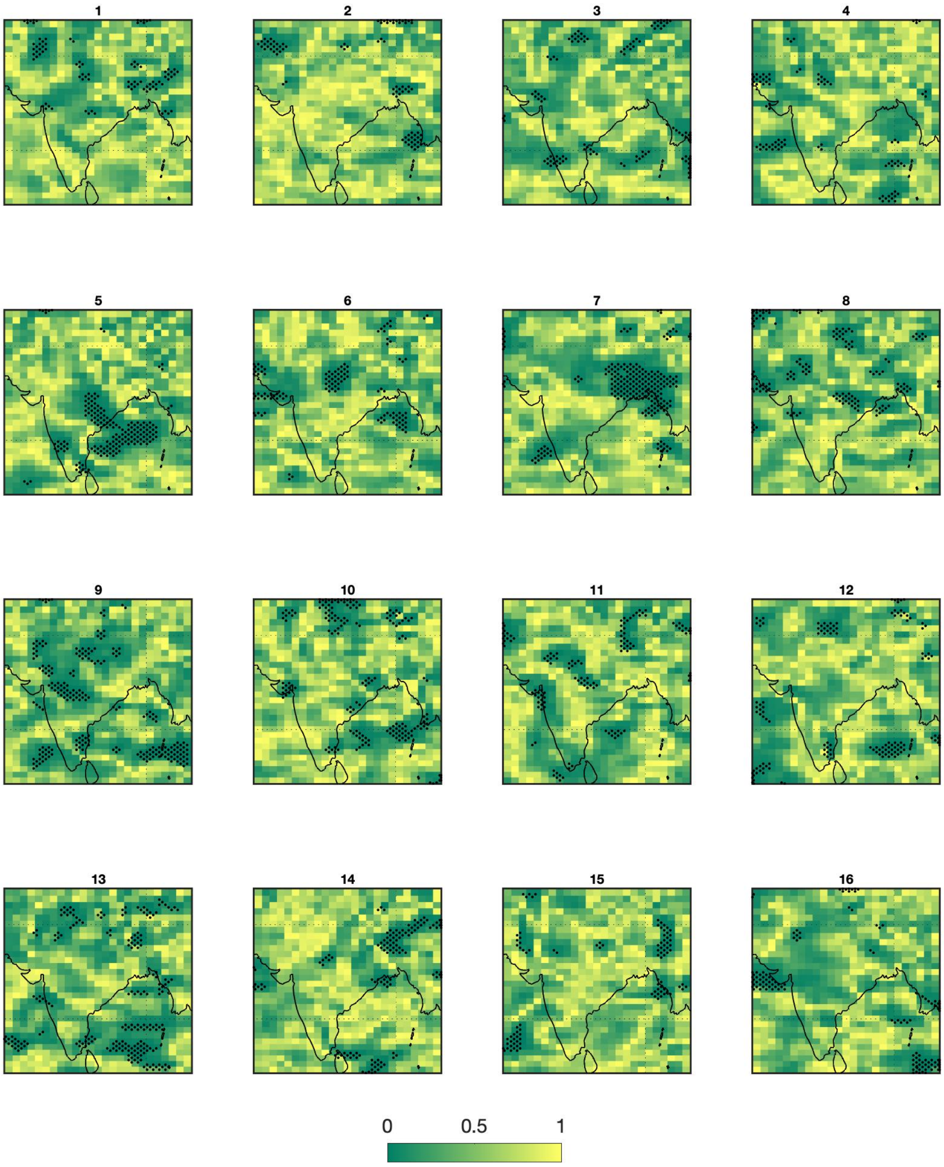

Figure S 2: Stamp diagram of p-values analogous to those in Fig. 1 (a), but here, instead of observational data, we consider single realisations of the CESM2-LE per diagram. Stippling indicates significance ($p < 0.05$). Areas of significance seem to be unrelated between different relaisations, signaling their falseness. See also Fig. 1 (c,d).

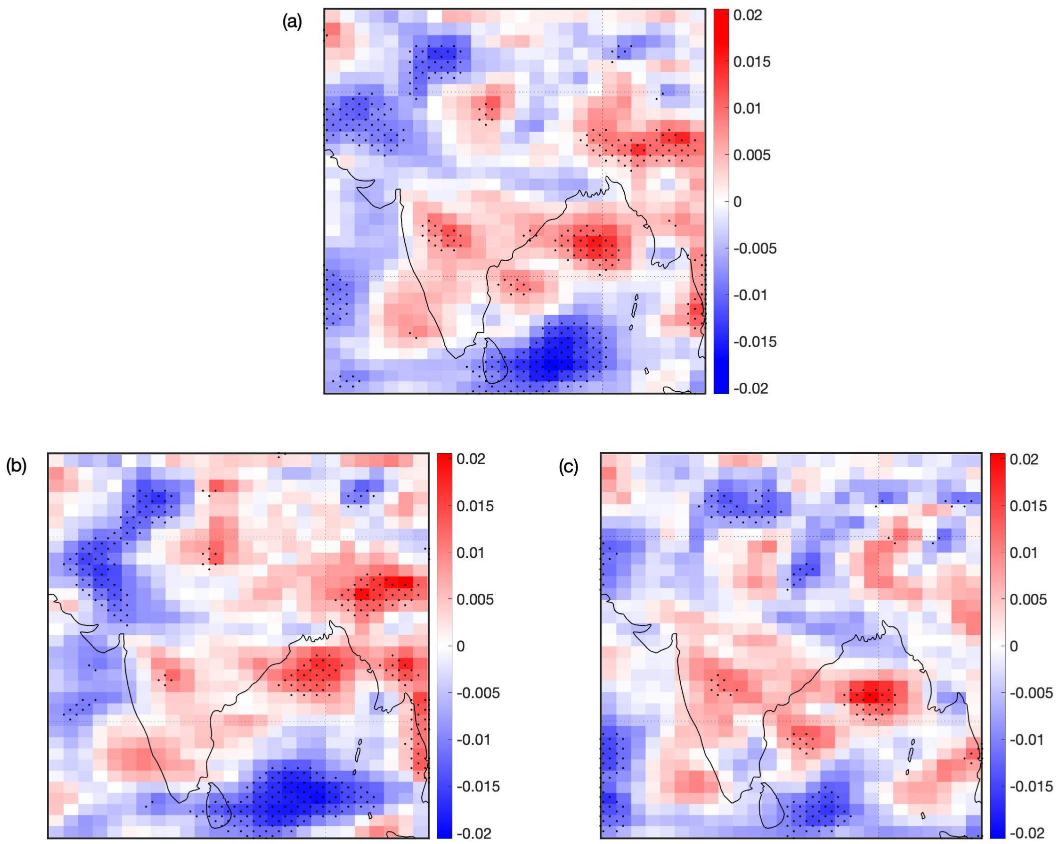

Figure S 3: Reference for Fig. 2 (a), panel (a) here being identical with that. Panels (b) and (c) show the same but for two nonoverlapping random sub-ensembles of equal size, which is to indicate that the detection in a small fraction of the gridpoints is not spurious, i.e., the detections are not to do with the finite confidence level.

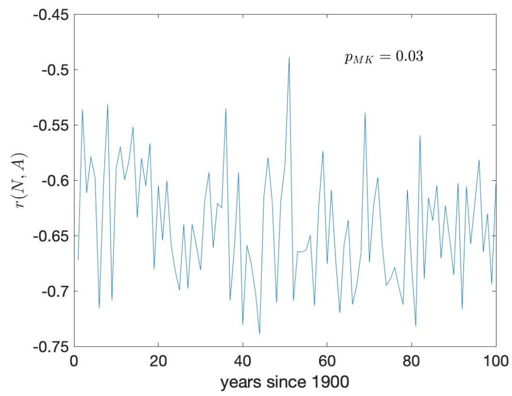

Figure S 4: Ensemble-wise correlation coefficient representing the conceptually sound [2, 3, 4] teleconnection climatology and its time-dependence, i.e., forced change. Following [4], the Mann-Kendall test of nonstationarity seems to detect a forced change with confidence ($p_{MK} = 0.03 < 0.05$). However, the detectable change seems to occur in the beginning of the 20th c., which might not be true forced response, but changes contingent on the initialisation of the CESM2-LE (see the second figure of the rebuttal [5] of [6]) in the process of approaching [7] the so-called climate snapshot/pullback attractor [8, 9, 10].

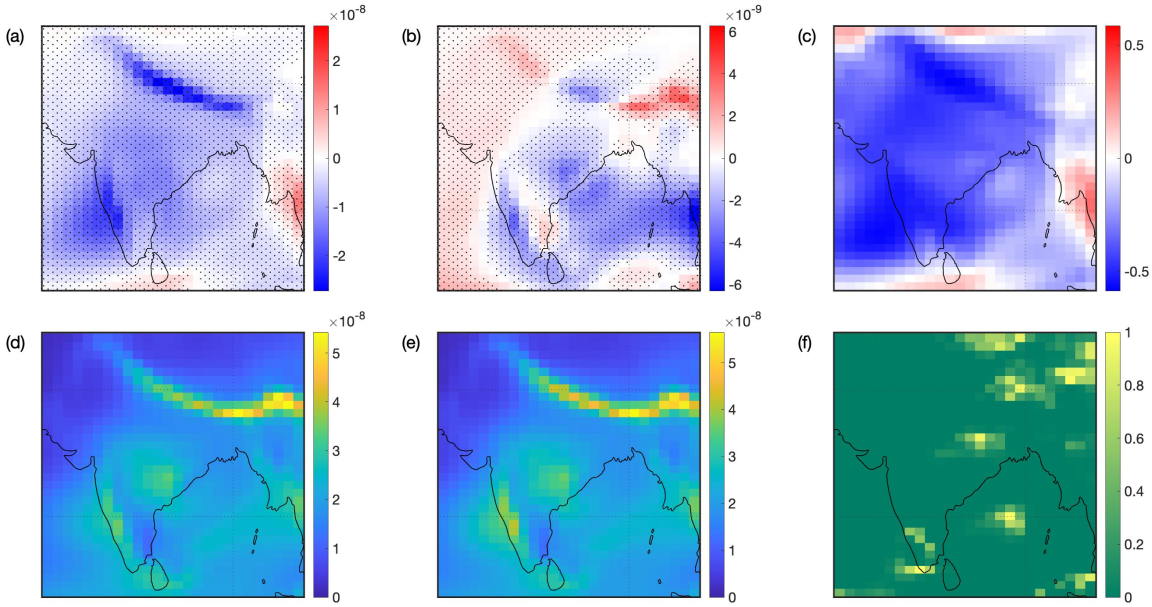

Figure S 5: Climatological ENSO-ISM teleconnection in view of a quadratic regression model R2 (6) fitted to the lumped annual anomaly data wrt. to time (20th c.) and CESM2-LE members (Methods). In the panels we show the regression coefficients (a) β_1, (b) β_2, (c) the cc r (compare to the pattern with the observational cc in Fig. S1 (a)), (d) RMSE, (e) variance of monsoon rain σ_M, (f) p-value of the test for heteroscedasticity [11], $\sigma_\xi = \sigma_\xi(N)$ eq. (6) (not actually considered for the regression model inference).

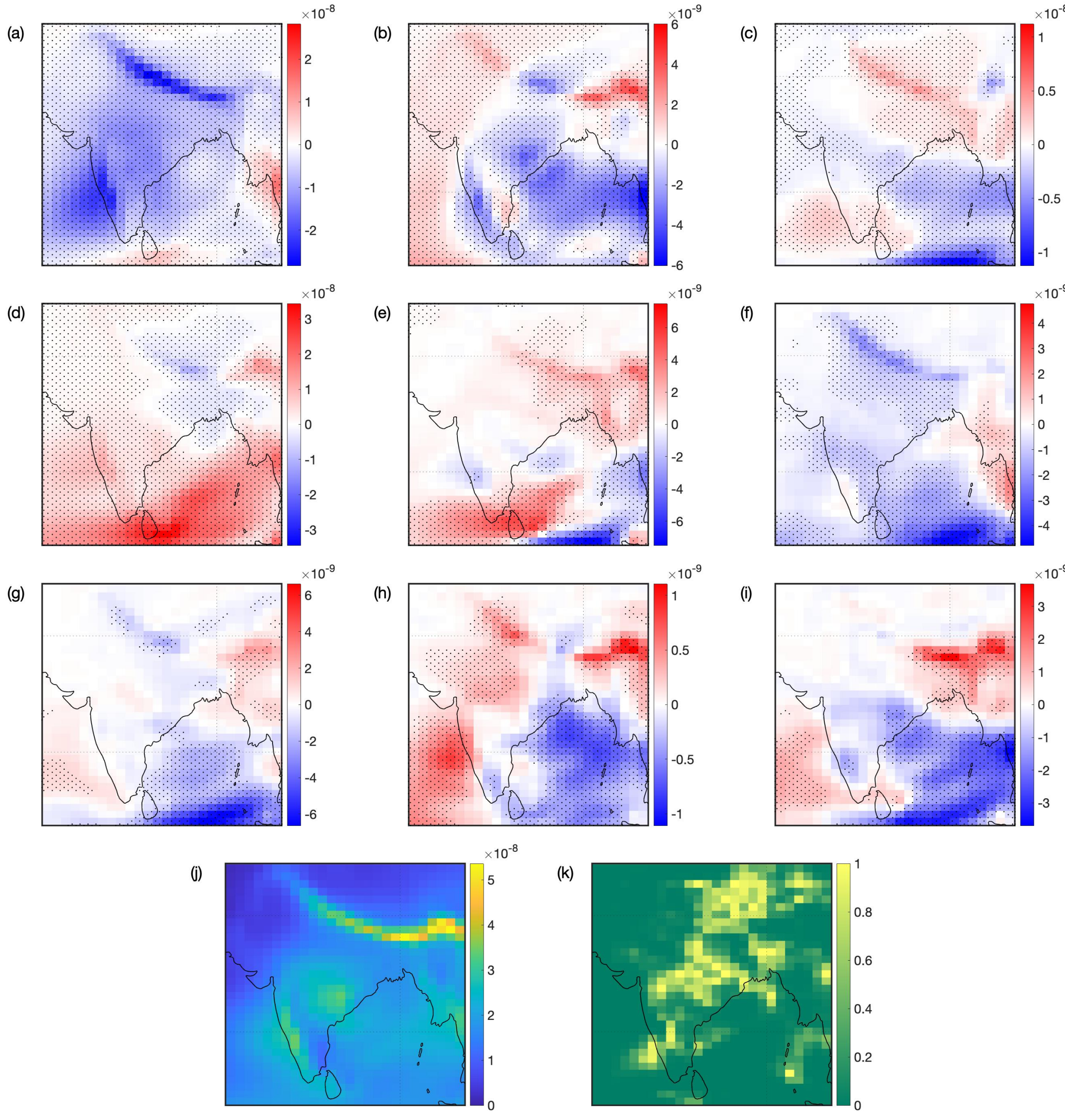

Figure S 6: Like in Fig. S5, but considering the 3-way relationship of ENSO-ISM-IOD*, as given by eq. (6). Panels show: (a) $\beta_{1,0}$, (b) $\beta_{2,0}$, (c) $\beta_{1,1}$, (d) $\beta_{0,1}$, (e) $\beta_{0,2}$, (f) $\beta_{2,1}$, (g) $\beta_{1,2}$, (h) $\beta_{3,0}$, (i) $\beta_{0,3}$, (j) RMSE, (k) p-value of the test for heteroscedasticity [11], $\sigma_\xi = \sigma_\xi(I^*)$.

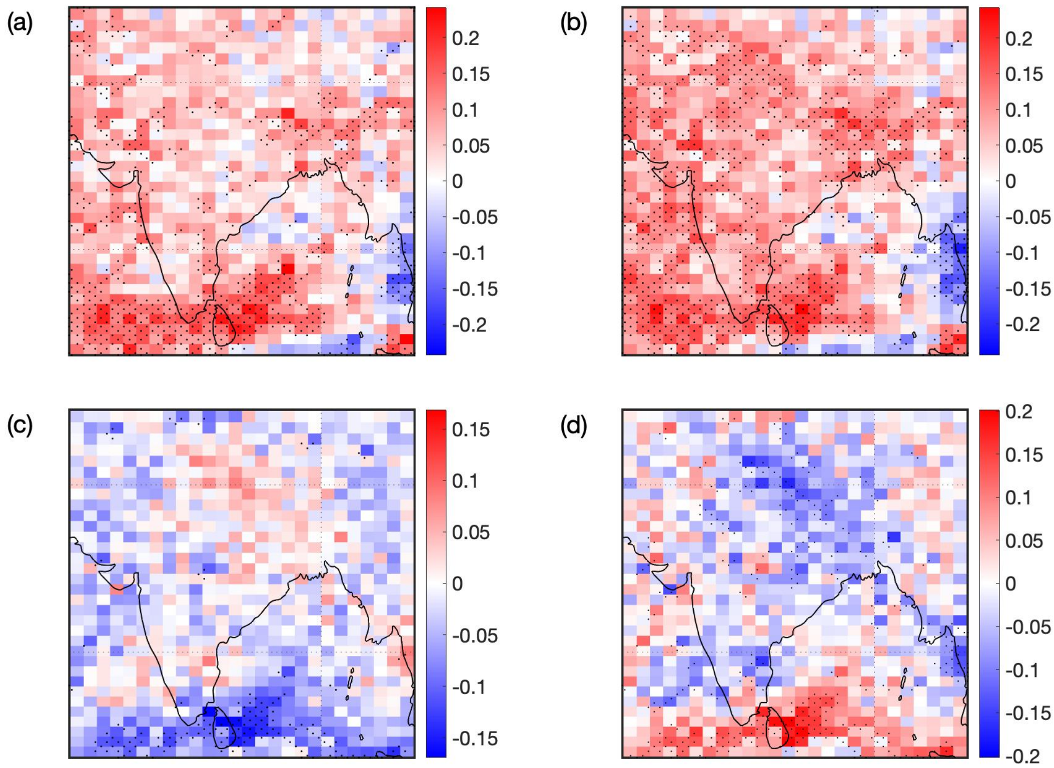

Figure S 7: Like Fig. 3 (a-d), but based on synthetic data.

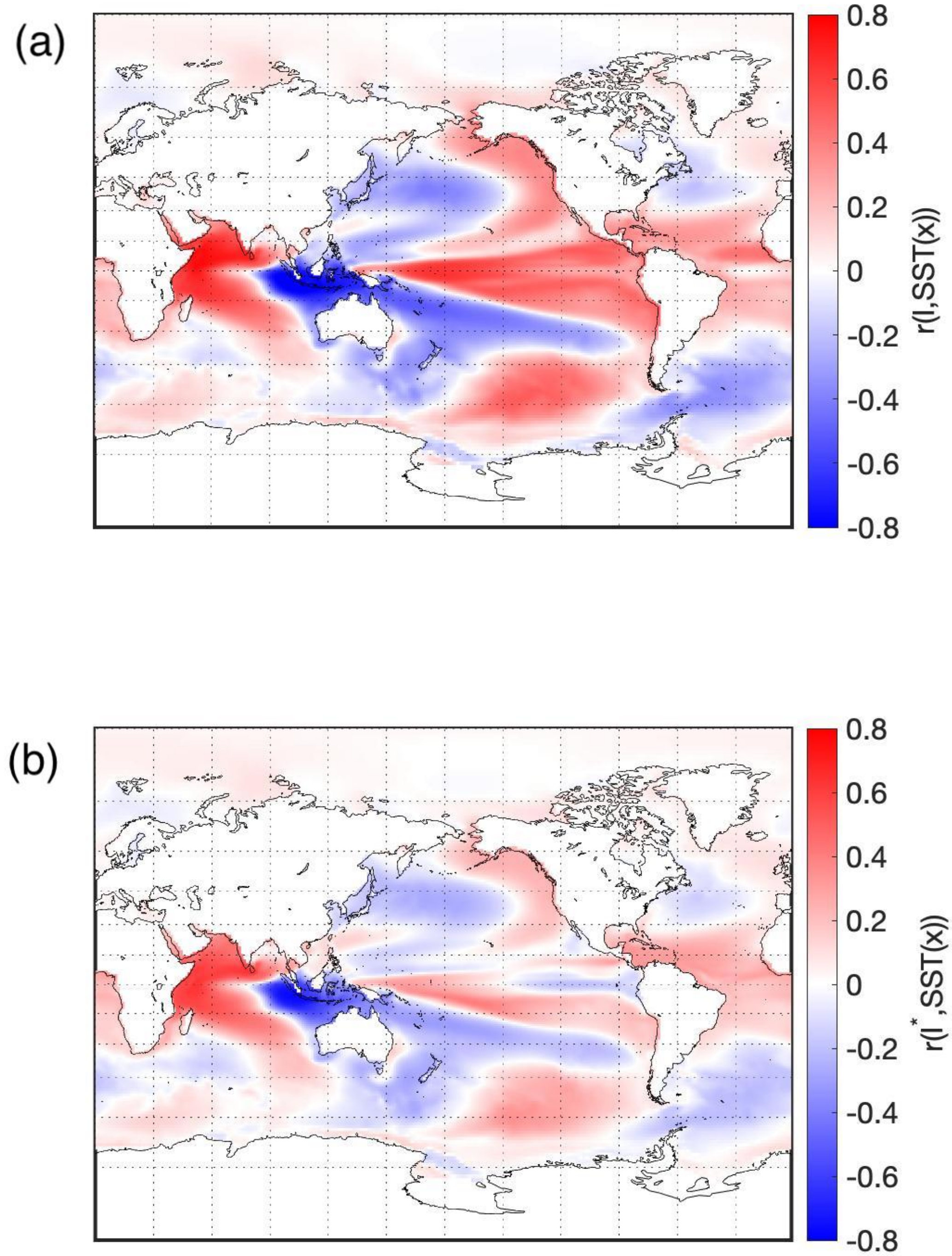

Figure S 8: Climatological correlation coefficients of JJA IOD and IOD* with global SST.

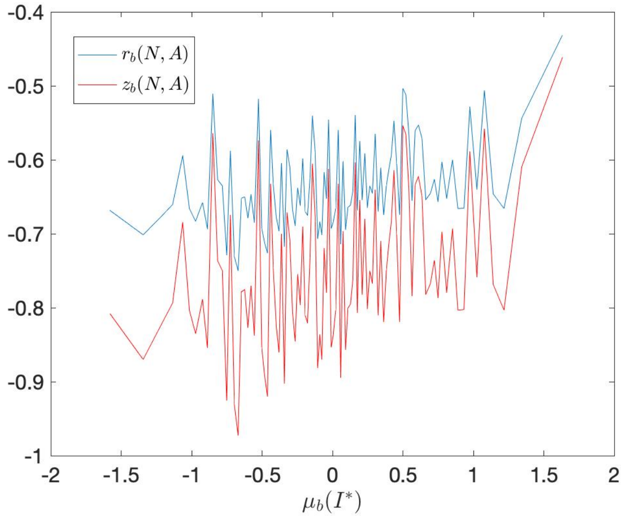

Figure S 9: Estimate of the conditional correlation coefficient (ccc) $r(N, A|I^*)$ from the 20th c. CESM2-LE data. The block size, i.e., the sample size from which a sample value of the ccc is calculated, is 100 (Methods).

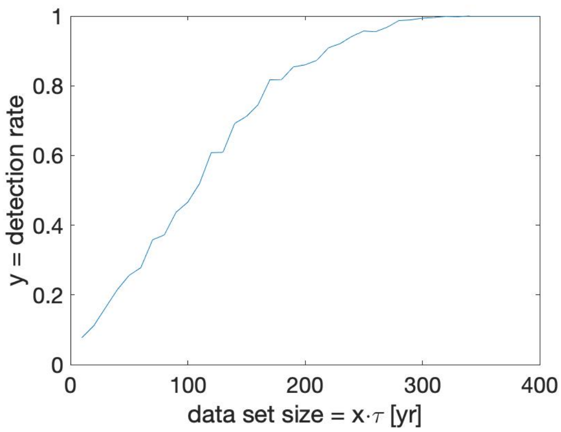

Figure S 10: Detectability of decadal Indian Ocean (IOD*, I^*) influence on the apparent ENSO-ISM teleconnection (Nino3.4-AISMR relationship), R_{r,I^*}, in terms of the likelihood of detection (significantly nonzero R_{r,I^*}) versus the data set size. This relationship underpins a probabilistic *time of emergence* (TOE) concept. E.g. for a 50% chance of detection, we need about 2000 years worth of data. Taking the same $RT/\tau = 500$ data points as used for Fig. 2, the likelihood of detection is estimated from a thousand random bootstrap samples.

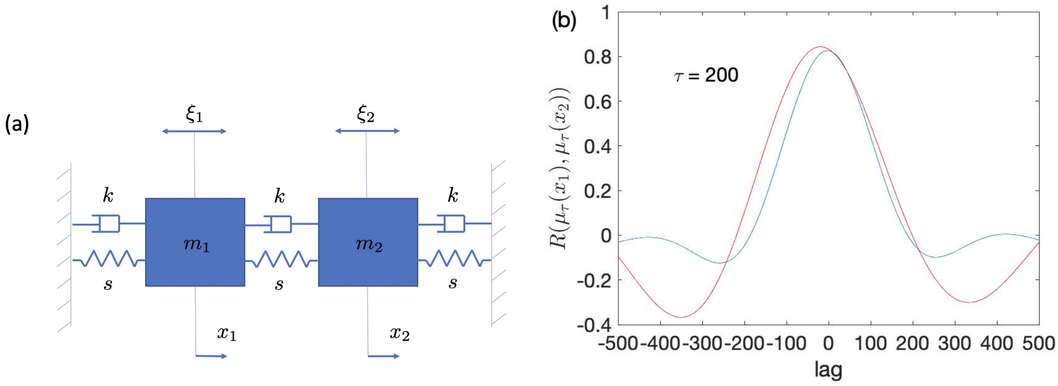

Figure S 11: The maximality of the correlation in a discrete mechanical system at some nonzero lag does not mean that the causality only goes one way. The sketch of the mechanical model in panel (a) depicts a two-body system (of masses m_1, m_2) suspended between the walls by springs (of stiffness s) and dampers (of damping coefficients k), driven by white noise random forces ξ_1, ξ_2 of equal variance. It is a basic exercise in engineering to establish the equations of motion [12]: $m_{1,2}\ddot{x}_{1,2}+2k\dot{x}_{1,2}-k\dot{x}_{2,1}+2sx_{1,2}-sx_{2,1} = \xi_{1,2}$. The causal influence can be quantified in this linear model by the coefficients upon dividing the respective equations my the masses $m_{1,2}$. Therefore, the balance in the causal influence can be shifted by having unequal masses. Panel (b) shows the symmetric and assymmetric lead-lag correlations of the positions of the masses for the scenarios of balanced and imbalanced causality, respectively.

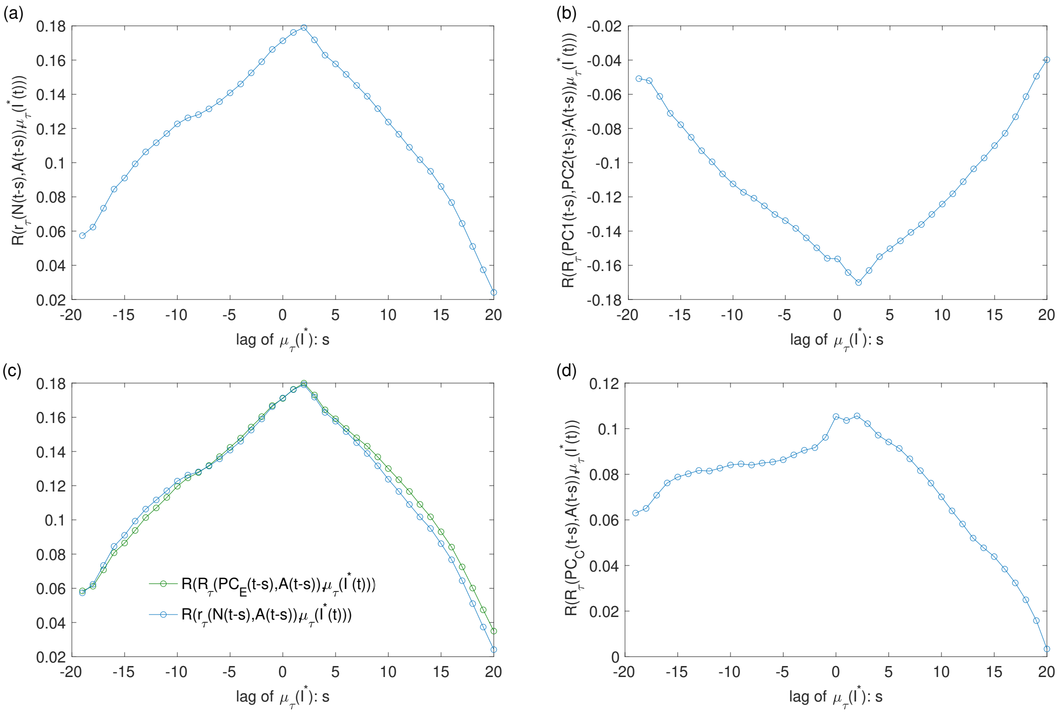

Figure S 12: Like Fig. 14 (a-c), but considering correlations directly – of different flavours wrt. the quantity used to represent ENSO. (a) The main variable that we use to describe ENSO: Niño3 (N). (b) Surface air temperature in the whole Equatorial Pacific, in the box (30°S, 30°N, 150°E, 295°E), whose variability is approximated considering only the first two EOFs. This is justifiable by Fig. 5 (a) of [13] showing the rapid decay of the fraction of explained variance with the mode number. We calculated the correlation coefficient belonging to the single Canonical Correlation Analysis mode when the *scalar* spatial mean of the AISMR is used as a target variable, in which case this correlation coefficient is precisely the coefficient of multiple correlation, as proven in the Supplementary Material of [13]. (c,d) Rotated EOFs, separately, the so-called Eastern and Central ENSO modes, and corresponding PCs defined [14] respectively as $PC_E = (PC1 + PC2)/2$ and $PC_C = (PC1 - PC2)/2$. The stronger influence of the E mode vs C is likely consistent with the findings of [15].

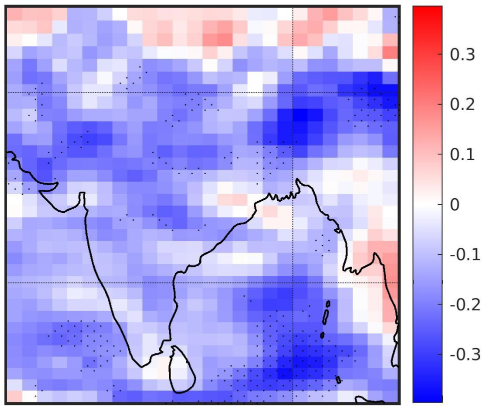

Figure S 13: Forced response of decadal apparent I^*-influence on the apparent ENSO-ISM teleconnection, corresponding to Fig. 3 (a). We show trends of $R_{r,I^*}(t) = r(r_\tau(N, M(x)|t), \mu_\tau(I^*))$ across approximately independent blocks, $t = k\tau,\ k = 1, \ldots, 10,\ \tau = 20$ [yr] (encompassing the 20th and 21st c. fully), obtained by linear regression. Stippling indicates the significance of the nonstationarity of the Fisher-transformed variable $\operatorname{atanh}(R)$ (subscripts omitted), instead.

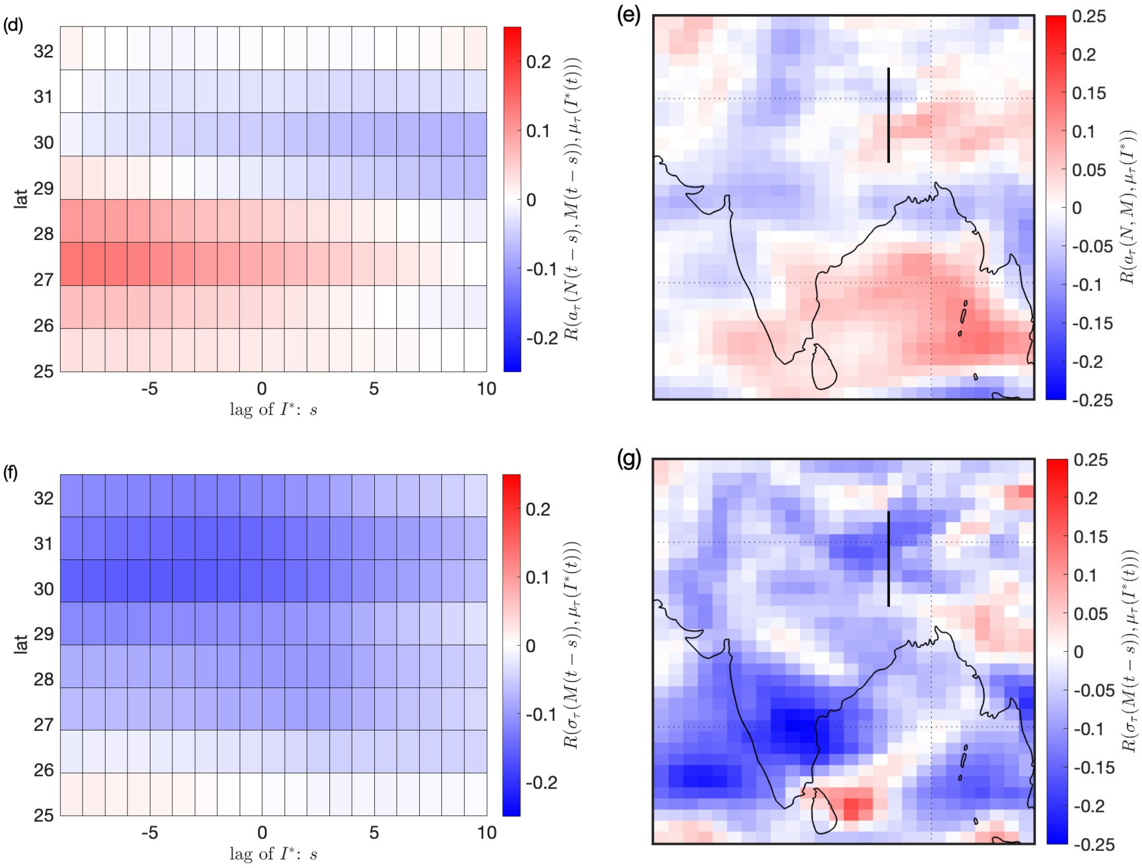

Figure S 14: Lead-lag correlations considered wrt. causality (Sec. 4.5), examining the attributability of the identified apparent influence like that of the Indian Ocean shown in Fig. 3 (a). Maximal lead/lags of $s = \mp 10$ [yr] are considered. Unlike in Fig. 2, here all possible windows of $\tau = 20$ [yr] are used for the calculation, achieving something like a sliding window smoothing. This results in slightly different patterns in panels (e) and (g) as compared to panels (b) and (d) of Fig. 3, respectively. In panels (e) and (g), vertical black lines highlight the gridpoints where the lead-lag correlation is evaluated as shown in panels (d) and (f), respectively.